PAPER

Electronic and magnetic properties of EuNi$_{2-\delta}$ Sb$_2$ structural variants

View the article online for updates and enhancements.

Electronic and magnetic properties of EuNi$_{2-\delta}$Sb$_2$ structural variants

W L Nelson[1,2]**, A S Jayasinghe**[3]**, D Graf**[1]**, S Latturner**[3]
and R E Baumbach[1,2,4]

[1] National High Magnetic Field Laboratory, Florida State University, Tallahassee, FL 32310, United States of America

[2] Department of Physics, Florida State University, Tallahassee, FL 32306, United States of America

[3] Department of Chemistry and Biochemistry, Florida State University, Tallahassee, FL 32306, United States of America

E-mail: baumbach@magnet.fsu.edu

Abstract
X-ray diffraction, magnetic susceptibility, magnetization, heat capacity and electrical resistivity results are reported for single crystals of two structural variants of EuNi$_{2-\delta}$Sb$_2$ that crystallize in the CaBe$_2$Ge$_2$ and ThCr$_2$Si$_2$-type structures. While the former occurs with a stoichiometric ratio, the latter exhibits a Ni site vacancy ($\delta = 0.36$). Both systems exhibit similar magnetic behavior at elevated temperatures, where there is an isotropic Curie–Weiss temperature dependence that indicates an antiferromagnetic exchange interaction between divalent europium ions, although it is stronger for the CaBe$_2$Ge$_2$-variant. At low temperatures, the differing structural environments that surround the Eu ions result in distinct ordering behavior. The CaBe$_2$Ge$_2$-variant orders antiferromagnetically near $T_{N1} = 6.9$ K and then undergoes a first order phase transition at $T_M = 4.6$ K. The ThCr$_2$Si$_2$-variant exhibits simpler behavior, with antiferromagnetic ordering at $T_{N2} = 5.6$ K. For both compounds, an applied magnetic field suppresses the ordering temperatures and induce metamagnetic phase transitions, while applied pressure causes the ordering temperatures to increase. From these results, EuNi$_{2-\delta}$Sb$_2$ emerges as a useful system in which to study the impact of structural variation on magnetism in a Eu-based metal.

Keywords: europium magnetism, BaAl$_4$ related crystal structures, antiferromagnetism

(Some figures may appear in colour only in the online journal)

1. Introduction

Eu-based materials that crystallize in structural variants of the BaAl$_4$ structure comprise a deep reservoir for novel physics [1–4]. Their behavior largely originates from the nearly half filled f-shell [Xe]4f^{7}6s^2, where the Eu valence features an instability between the 2+ ($J = 7/2$) and 3+ ($J = 0$) configurations. Like the nearly empty (Ce) and nearly full (Yb) f-shell analogues, this sets the stage for structural, electronic and magnetic instabilities that can produce novel spin and charge order, valence fluctuations, and Kondo lattice-like physics [5–8]. For instance, EuPd$_2$Si$_2$ undergoes a temperature driven

valence transition at $T_V = 200$ K [9, 10] while EuRh$_2$Si$_2$ is an antiferromagnet where applied pressure abruptly changes the Eu valence from 2+ to 3+ near 1 GPa [11–13]. EuNi$_2$P$_2$ [14, 15], EuIr$_2$Si$_2$ [16], EuPt$_2$Si$_2$ [17] and EuCu$_2$(Ge$_{1-x}$Si$_x$)$_2$ [18] also exhibit behavior that resembles that of a typical heavy fermion Kondo lattice. Based on such observations, it is appealing to organize these materials within a Doniach-like phase diagram [4, 19], where tuning parameters such as applied pressure and/or chemical substitution adjust both the Eu valence and the relative strengths of the RKKY and Kondo interactions [20–23]. On the other hand, the phase diagrams of Eu-based intermetallics are often dominated by the Eu valence instability, which may preempt or compete with Kondo lattice physics. Thus, it remains an open question whether novel

[4] Author to whom any correspondence should be addressed.

phenomena (quantum criticality and superconductivity) that are analogous to what is observed in Ce-based materials can appear in Eu-based analogues.

Here we report results for single crystals of $EuNi_{2-\delta}Sb_2$ that are produced using a molten lead flux, where the absence (or presence) of phosphorus in the melt results in the formation of specimens with either the $CaBe_2Ge_2$- or $ThCr_2Si_2$-type structure. These structures are similar, but are distinguished by the stacking order of elements along the c-axis, which results in different space groups; $I4/mmm$ for the $ThCr_2Si_2$ variant and $P4/nmm$ for the $CaBe_2Ge_2$ variant. For these Eu compounds, the unit cell volume of the $CaBe_2Ge_2$ variant is slightly larger than that of the $ThCr_2Si_2$ one and is also compressed along the c-axis. Also important is that while the former case exhibits complete filling of the crystallographic sites, the latter shows a significant vacancy on the Ni site ($\delta = 0.36$). This structural/site-filling variation is of interest because, while there are many lanthanide-based materials that can crystallize in either the $ThCr_2Si_2$ or $CaBe_2Ge_2$ structures [1, 24], it is unusual to be able to compare the impact of such variation in similar stoichiometries.

Magnetic susceptibility, heat capacity, and electrical resistivity measurements reveal that both structures exhibit metallic behavior and magnetism that originates from divalent europium. The $CaBe_2Ge_2$-variant shows two phase transitions at $T_{N1} = 6.9$ K and $T_M = 4.3$ K (first order), both of which have an antiferromagnetic character, while the $ThCr_2Si_2$-variant orders antiferromagnetically at $T_{N2} = 5.6$ K. For both compounds, magnetic fields suppress the ordering temperatures and induce metamagnetic phase transitions. Applied pressure also causes the ordering temperatures to increase in a manner that is consistent with a strengthening RKKY interaction due to compression of the unit cell volume. These results highlight the $EuNi_{2-\delta}Sb_2$ structural variants as environments in which to study the impact of structural variation on magnetism.

2. Experimental methods

Single crystals of $EuNi_2Sb_2$ were grown using elements with purities >99.9% in a molten lead flux [25]. Two variations of this method were used. In the first, which produces crystals with the $CaBe_2Ge_2$-type structure, the starting elements were loaded into a 5 ml alumina crucible with the molar ratio 0.29 (Eu):1 (Ni):1 (Sb):20 (Pb). In the second, which produces crystals with the $ThCr_2Si_2$-type structure, the starting elements were loaded into a 5 ml alumina crucible in the same ratio, except the antimony was partially replaced by phosphorus [0.29 (Eu):1 (Ni):0.6 (Sb):0.4 (P):20 (Pb)]. In both cases, the Pb was split such that half of it was above the reactants and half was below. The crucibles were then sealed under vacuum in a quartz tube, heated to 850 °C at a rate of 50 °C h^{-1}, with one hour dwells at 300 °C and 600 °C. After three hours at 850 °C, the ampules were cooled to 650 °C at a rate between 2 and 5 °C h^{-1}. The excess flux was removed by centrifuging the tubes, after which square-faced platelets with typical dimensions of several millimeters in width and 0.5 to 1 mm thickness were collected (figure 1). As shown in (figure 1 left),

unusually large crystals are also sometimes produced. Finally, the residual flux was removed by etching the crystals in a mixture of dilute hydrogen peroxide (3 percent H_2O_2, 97 percent H_2O) and glacial acetic acid. Upon polishing, it was revealed that those that form in the $ThCr_2Si_2$-type structure from melts with P often have Pb inclusions.

Semi-quantitative elemental analysis data were obtained using an FEI NOVA 400 scanning electron microscope (SEM) with energy dispersive x-ray spectroscopy (EDS) capabilities. Selected crystals were oriented on carbon tape perpendicular to the electron beam. The crystals were analyzed using a 30 kV accelerating voltage and an accumulation time of 50 s. In order to obtain complete structural data small fragments were cleaved from single crystals, coated in oil, placed in a MiTeGen tip and mounted on a Bruker D8 Quest single-crystal x-ray diffractometer equipped with Mo K-α radiation ($\lambda = 0.7107$ Å). Data were collected at room temperature with the Bruker software package [26], and peak intensities were corrected for Lorentz, polarization, and background effects using the Bruker APEX III software [27]. An empirical absorption correction was applied using the program SADABS and the structure solution was determined by direct methods and refined on the basis of F^2 for all unique data using the SHELXTL program suite [28].

Magnetization $M(T, H)$ measurements were carried out for single crystals at temperatures $T = 1.8$–300 K under an applied magnetic field of $H = 0.5$ T for H applied both parallel ($\parallel$) and perpendicular ($\perp$) to the c axis using a Quantum Design VSM Magnetic Property Measurement System. The heat capacity C was measured for $T = 0.4$–20 K and the electrical resistivity ρ was measured in a four-wire configuration for temperatures $T = 1.8$–300 K and $H < 9$ T using a Quantum Design Physical Property Measurement System. Electrical resistivity measurements were also performed using a dilution refrigerator for $T > 10$ mK and $H < 18$ T. $\rho(T)$ measurements under applied pressure were performed using a piston cylinder pressure cell with Daphne 7474 oil as the pressure transmitting medium. The pressure was determined by the shift in ruby fluorescence peaks as measured below $T = 10$ K.

3. Results

Results from single crystal x-ray diffraction measurements are summarized in tables 1 and 2, where we compare specimens with the $CaBe_2Ge_2$ (space group $P4/nmm$) and $ThCr_2Si_2$ (space group $I4/mmm$) structures (figure 1). The $ThCr_2Si_2$ and $CaBe_2Ge_2$ structures can be viewed as two substitutional variants of the parent $BaAl_4$ structure, with different 'coloring' patterns leading to different symmetries [1]. Viewed as stacking of layers, the higher symmetry ($I4/mmm$) $ThCr_2Si_2$ type is built of layers of each element in the order Ni–Sb–Eu–Sb–Ni. This maintains the body centering and inversion symmetry at the Eu site. The lower symmetry ($P4/nmm$) $CaBe_2Ge_2$ is built with a Ni–Sb–Eu–Ni–Sb layer stacking, which eliminate the body centering of the structure and the inversion symmetry at the rare earth position. Also important is that the $CaBe_2Ge_2$ structure has two crystallographically unique
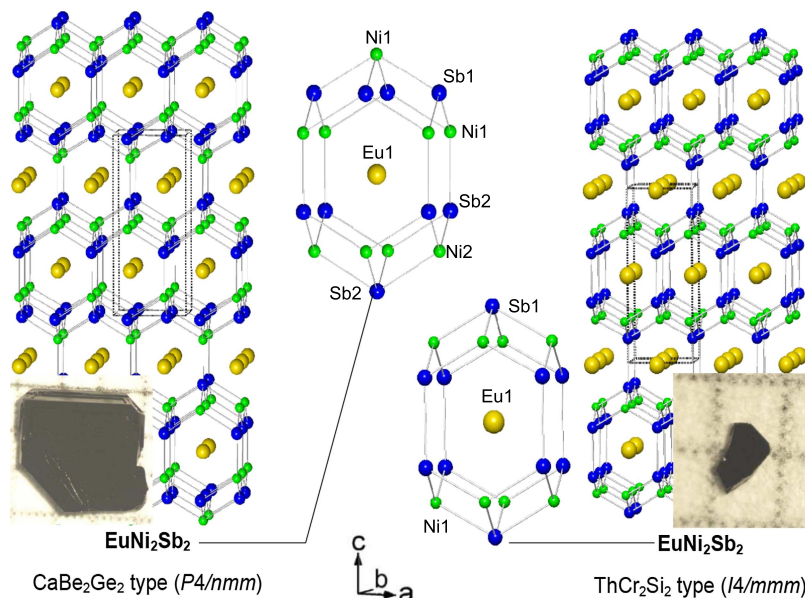
Figure 1. Crystal structures for the EuNi$_2$Sb$_2$ variants viewed down the *a* axis and the local coordination of the europium sites. Europium, antimony, and nickel are represented by yellow, blue, and green spheres, respectively. Insets show crystalline samples for each structure type on mm grid paper.

Table 1. Selected crystallographic data for the EuNi$_2$Sb$_2$ structural variants from single crystal x-ray diffraction data collected at room temperature.

	EuNi$_2$Sb$_2$	EuNi$_{1.64}$Sb$_2$
Structure type	CaBe$_2$Ge$_2$	ThCr$_2$Si$_2$
Space group	*P4/nmm*	*I4/mmm*
Molar mass (g mol^{-1})	512.88	491.74
Density (g cm^{-3})	8.319	8.105
Lattice constants (Å)	$a = 4.4886(8)$	$a = 4.3536(13)$
	$c = 10.1628(19)$	$c = 10.631(3)$
	$c/a = 2.4418$	$c/a = 2.2641$
Volume (Å^3)	$V = 204.76(8)$	$V = 201.50(13)$
Z	2	2
μ (mm^{-1})	36.903	35.866
F (000)	442	422
Crystal size (μm)	$60 \times 40 \times 40$	$40 \times 40 \times 20$
Data θ (°) range	4.010–34.625	3.833–34.753
Limiting indices	$-6 \leqslant h \leqslant 7$	$-6 \leqslant h \leqslant 6$
	$-7 \leqslant k \leqslant 7$	$-6 \leqslant k \leqslant 6$
	$-15 \leqslant l \leqslant 7$	$-16 \leqslant l \leqslant 16$
Reflections/unique	4406/299	2251/153
R (int)	0.0359	0.0348
GOF	1.245	1.121
Final *R* indices	$R_1 = 0.0219$	$R_1 = 0.0226$
$I > 2\sigma(I)$	w$R_2 = 0.0522$	w$R_2 = 0.0587$
R indices (all data)	$R_1 = 0.0227$	$R_1 = 0.0230$
	w$R_2 = 0.0522$	w$R_2 = 0.0587$
Largest diff. peak/hole	2.520/-2.452	1.354/-1.681

Table 2. Atomic coordinates and occupancies from single crystal x-ray diffraction data for the EuNi$_2$Sb$_2$ structural variants.

	Wyc. sym.	Occ.	x	y	z	U_{eq}
EuNi$_2$Sb$_2$						
Eu1	2c	1	0.25	0.25	0.242 77(3)	0.0101(1)
Ni1	2a	1	0.25	0.25	0.623 19(7)	0.0123(2)
Ni2	2c	1	0.75	0.25	0	0.0150(2)
Sb1	2b	1	0.75	0.25	0.5	0.0094(2)
Sb2	2c	1	0.25	0.25	0.873 35(4)	0.0111(2)
EuNi$_{1.64}$Sb$_2$						
Eu1	2a	1	0	0	0	0.0123(3)
Ni1	4d	0.819	0	0.5	0.25	0.0245(4)
Sb1	4e	1	0	0	0.359 75(5)	0.0235(3)

Ni and Sb sites. For the ThCr$_2$Si$_2$ variant, refinement of the x-ray diffraction data and EDS measurements reveal that the nickel site is partially occupied (82%), similar to earlier observations by Jeitschko [24, 29]. With the CaBe$_2$Ge$_2$

structure, EuNi$_2$Sb$_2$ is a previously unreported example of the series with the formula LnNi$_{2-x}$Sb$_2$ (Ln = La, Ce, Pr, Nd, Sm, Gd, Tb, Dy, Ho, Er) [24], but here the Ni site is fully occupied.

Thus, EuNi$_{1.64}$Sb$_2$ (*I4/mmm*) and EuNi$_2$Sb$_2$ (*P4/nmm*) have similar unit cell parameters, but the coordination around the europium sites is different. The europium ions in the former (Tet-I) are coordinated by a compressed cube of eight symmetry equivalent antimony sites at a distance of 3.4205(9) Å, and further by eight nickel atoms at 3.4354(7) Å. In the Tet-P EuNi$_2$Sb$_2$ structure, the europium site is coordinated on one side by four nickel atoms [Eu–Ni(2) bond distance 3.3353(5) Å] and on the other side by four antimony atoms [Eu–Sb(2) bond distances 3.3862(6) Å]. The Ni–Sb bond lengths that surround the Eu site range from

Table 3. Selected bond distances in angstroms for EuNi$_2$Sb$_2$ (CaBe$_2$Ge$_2$-type) and EuNi$_{1.64}$Sb$_2$ (ThCr$_2$Si$_2$-type) from single crystal x-ray diffraction data.

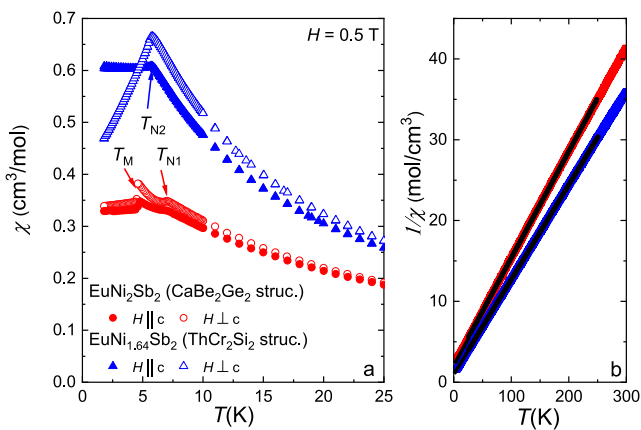| **EuNi$_2$Sb$_2$**	
Eu(1)–Sb(1)	3.4454(5)
Eu(1)–Sb(2)	3.3862(6)
Eu(1)–Ni(1)	3.4539(4)
Eu(1)–Ni(2)	3.3353(5)
Sb(1)–Ni(1)	2.5699(5)
Sb(2)–Ni(1)	2.5423(10)
Sb(2)–Ni(2)	2.5872(4)
Sb(1)–Sb(1)	3.1739(6)
EuNi$_{1.64}$Sb$_2$	
Eu(1)–Sb(1)	3.4205(9)
Eu(1)–Ni(1)	3.4354(7)
Sb(1)–Ni(1)	2.4698(7)
Sb(1)–Sb(1)	2.9821(14)

Figure 2. (a) Zoom of magnetic susceptibility $\chi(T) = M/H$ vs temperature T collected in a magnetic field $H = 0.5$ T for the EuNi$_2$Sb$_2$ variants, focusing on the T region near the phase transitions T_{N1}, T_M, and T_{N2}. H was applied parallel ($\parallel$) and perpendicular ($\perp$) to the c axis. (b) $1/\chi(T)$ vs T where solid lines are Curie–Weiss fits to the data. Only $H \parallel c$ is shown because there is negligible anisotropy for $T > 30$ K.
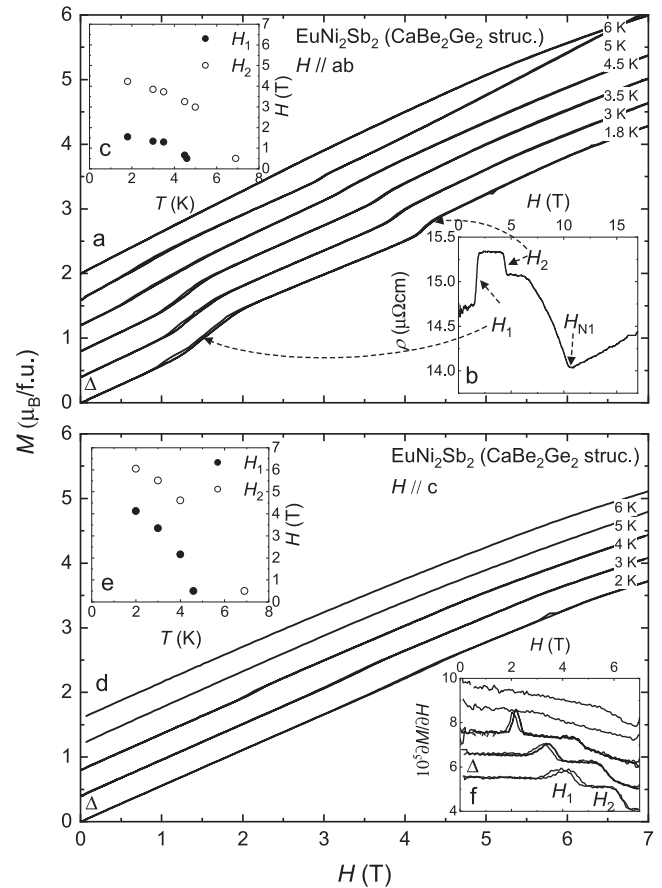

Figure 3. (a) Magnetization M vs magnetic field H at several temperatures T for H applied parallel ($\parallel$) to the ab crystallographic plane for the CaBe$_2$Ge$_2$ structural variant. Metamagnetic phase transitions are observed at H_1 and H_2. For clarity, the curves are offset vertically by the value $\Delta = 0.4$ μ_B/f.u. (b) The electrical resistivity $\rho(H)$ at $T = 10$ mK for electrical current and H applied in the ab-plane. In addition to the features at H_1 and H_2, there is a sharp feature at $H_{N1} = 10.5$ T. (c) T–H phase diagram constructed from the metamagnetic phase transitions H_1 and H_2 for $H \parallel ab$. (d) $M(H)$ at several T for $H \parallel c$. (d) Derivative of the magnetization $\partial M/\partial H$ vs H showing the subtle features at the metamagnetic phase transitions H_1 and H_2. (e) T–H phase diagram constructed from the metamagnetic phase transitions H_1 and H_2 for $H \parallel c$.

2.5423(10)–2.5872(4) Å; this is distinctly shorter than the corresponding Sb–Sb bonds in the *I4/mmm* structure [2.982(1) Å], which accounts for the difference in the c-axis length of the two structures. Additional selected bond distances are listed in table 3.

The magnetic susceptibility $\chi(T)$ data for both structural variants are presented in figure 2, where Curie–Weiss temperature dependencies [$\chi(T) = C/(T - \theta)$] with negligible anisotropies are observed. Fits to the data yield $\theta = -15$ K and $\mu_{\text{eff}} \approx 7.5$ μ_B for the CaBe$_2$Ge$_2$ variant and $\theta = -8$ K and $\mu_{\text{eff}} \approx 8$ μ_B for the ThCr$_2$Si$_2$ variant. In both cases the signs of θ suggest that the magnetic exchange interaction is antiferromagnetic (but stronger for the CaBe$_2$Ge$_2$ case), while the effective magnetic moments are consistent with the Eu ions being in (or nearly in) the divalent state ($J = 7/2$, $\mu_{\text{eff}} \approx 7.9$ μ_B), although μ_{eff} for the CaBe$_2$Ge$_2$

variant is slightly reduced from the expected value. The nearly isotropic Curie–Weiss behavior at elevated temperatures is consistent with the expectation from Hund's rules that the orbital angular momentum quantum number $L = 0$, although below $T \approx 30$ K a small amount of anisotropy develops. At low temperatures there are clear differences in behavior between the variants. While the CaBe$_2$Ge$_2$ version shows an antiferromagnetic-like decrease near $T_{N1} = 6.9$ K that is followed by a sharp first order like feature near $T_M = 4.8$ K that further reduces χ, the ThCr$_2$Si$_2$ version exhibits an anisotropic antiferromagnetic phase transition at $T_{N2} = 5.9$ K. For both cases, this behavior is similar to what is seen for the closest chemical variants: e.g., EuPd$_2$Sb$_2$ (CaBe$_2$Ge$_2$) exhibits two magnetic phase transitions [30] while EuNi$_2$As$_2$ (ThCr$_2$Si$_2$) exhibits a single antiferromagnetic transition [31, 32].

The field dependent magnetization $M(H)$ data at several temperatures are summarized in figures 3 and 4. For the
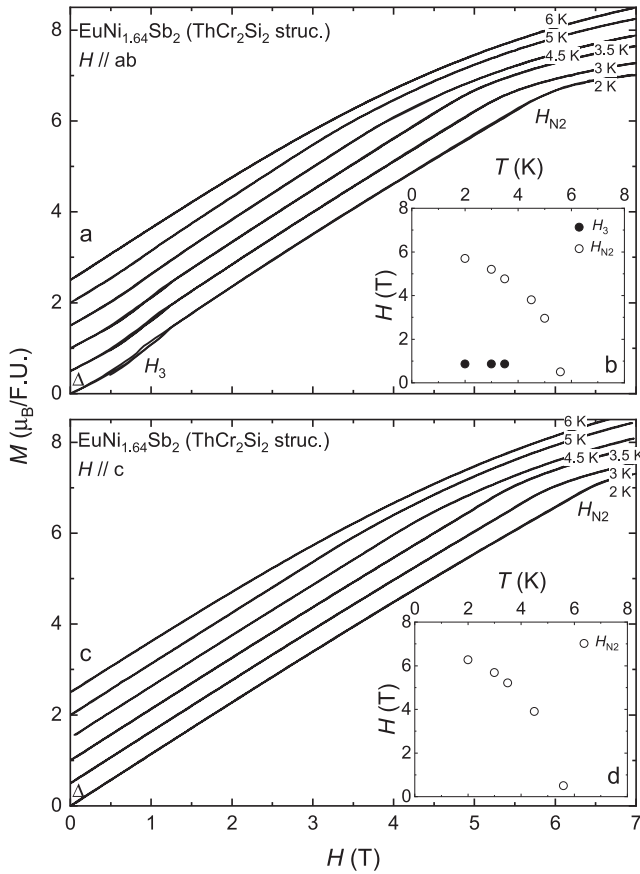
Figure 4. (a) Magnetization M vs magnetic field H at several temperatures T for H applied parallel ($\parallel$) to the ab crystallographic plane for the ThCr$_2$Si$_2$ structural variant. Metamagnetic phase transitions are observed at H_3 and H_{N2}. For clarity, the curves are offset vertically by the value $\Delta = 0.5$ μ_B/f.u. (b) T–H phase diagram constructed from the metamagnetic phase transitions H_3 and H_{N2} for $H \parallel ab$. (c) $M(H)$ at several T for $H \parallel c$. (d) T–H phase diagram constructed from the metamagnetic phase transition H_{N2} for $H \parallel c$.

Figure 5. (a) Heat capacity divided by temperature C/T vs T for the EuNi$_2$Sb$_2$ variants. (b) The thermal relaxation curve for the CaBe$_2$Ge$_2$ variant collected near T_M, where the curvature of the T-rising trace reveals a latent heat. For comparison, a typical $T(t)$ trace that was collected away from T_M at 5 K is also shown. (c) The 4f contribution to the entropy $S_{4f}(T)$ calculated as described in the text. The dotted line represents the entropy that is expected for the divalent europium Hund's rule multiplet. (d) $C(T)$ for the CaBe$_2$Ge$_2$ variant collected over a broad temperature range. The solid blue line is fit to the data using the Debye function, as described in the text.

CaBe$_2$Ge$_2$ variant there is little anisotropy in the magnitude of M at any temperature [panels (a) and (d)], but there are several metamagnetic phase transitions that appear at the fields H_1 and H_2 depending on the field orientation. Importantly, for all field orientations, the magnetization values do not reach the Hund's rule divalent europium magnetic moment ($M_{sat} = 7$ μ_B/Eu) up to $H = 7$ T, suggesting that larger magnetic fields would drive additional spin reconfigurations to saturate the full moment. In order to explore this possibility, electrical resistivity $\rho(H)$ measurements were performed for $T = 10$ mK and magnetic fields up to $H = 18$ T with the electrical current and H applied in the ab plane (figure 3(b)). Here, sharp features are first observed at H_1 and H_2, and an additional cusp is seen near $H_{N1} = 10.5$ T. This likely represents the field that is needed to fully polarize the f-electrons and cross the field driven antiferromagnetic phase boundary. The resulting T–H phase diagrams are shown in figures 3(c) and (e). Results for the ThCr$_2$Si$_2$ variant are somewhat different (figure 4). Again, there is evidence for several metamagnetic phase transitions, but at different fields (H_3 and H_{N2}). The resulting T–H phase diagrams are shown in figures 4(b) and (d). For both field
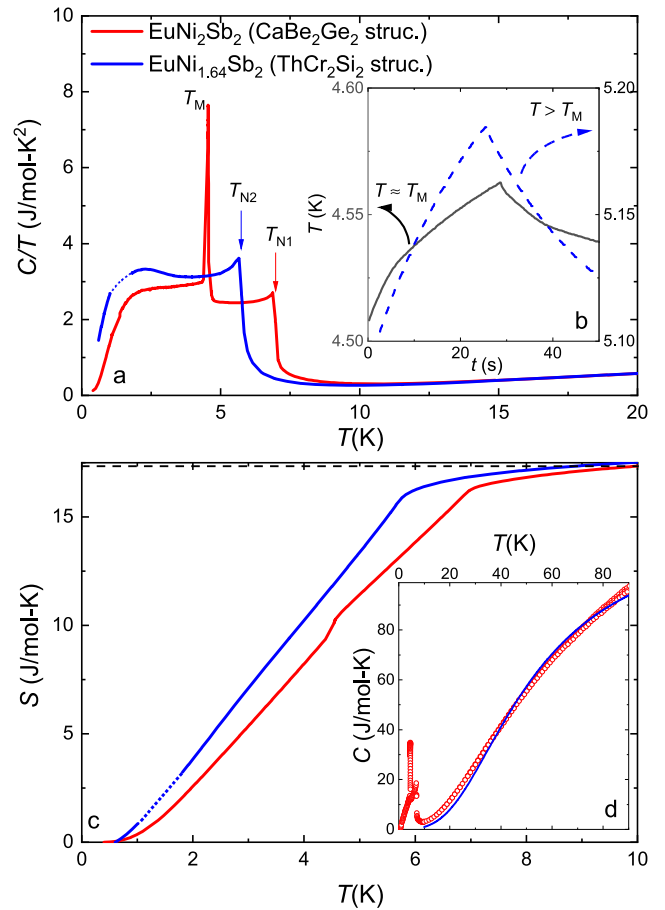
directions, the magnetization saturates towards the expected 7 μ_B/Eu near 7 T, suggesting that there are no further transitions at larger fields. We point out that the differences between H_{N1} and H_{N2} are consistent with the observation that θ (i.e., the magnetic exchange interaction strength) for the CaBe$_2$Ge$_2$ variant is roughly double that of the ThCr$_2$Si$_2$ variant.

The specific heat divided by temperature C/T data are shown in figure 5. For temperatures above the ordered states the heat capacity is similar for both compounds showing that the lattice contributions are nearly identical. In order to model the lattice contribution, $C(T)$ for the CaBe$_2$Ge$_2$ variant was fitted using the Debye function for $T > T_{N1}$ (figure 5(d)). This yields a Debye temperature $\theta_D \approx 210$ K, which is comparable to the value that was earlier found for the non-4f electron containing LaPd$_2$Sb$_2$ [33]. The primary antiferromagnetic phase transitions appear as second order-like features at T_{N1} and T_{N2} while the lower temperature phase transition at T_M for the CaBe$_2$Ge$_2$ variant appears as a sharp first order peak. Here, the
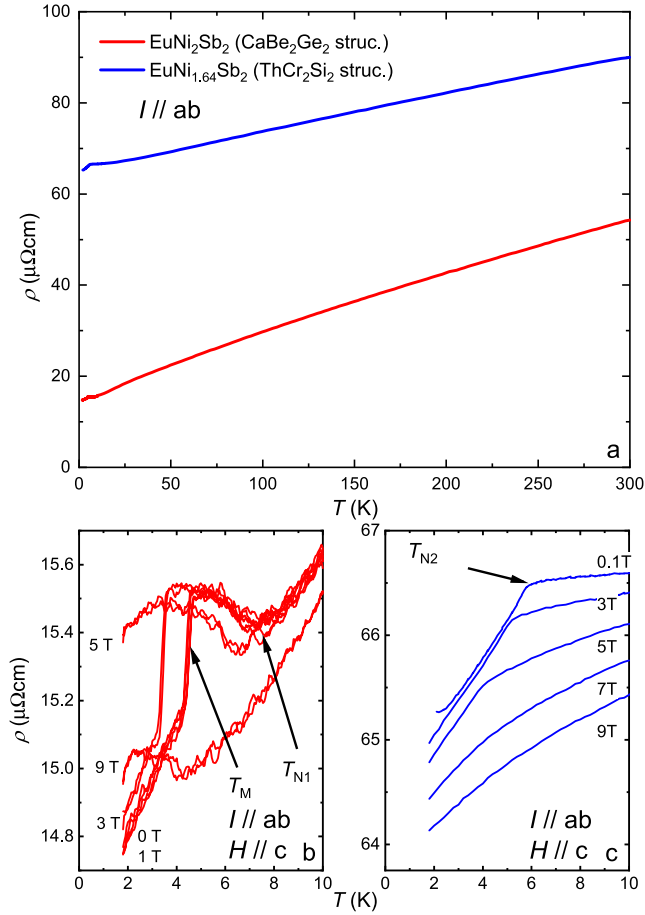
Figure 6. (a) Electrical resistivity ρ vs temperature T for the EuNi$_2$Sb$_2$ variants where the electrical current I is applied in the *ab* crystallographic plane. (b) Low temperature $\rho(T)$ under applied magnetic fields $H = 0$–9 T applied parallel to the *c*-axis for the CaBe$_2$Ge$_2$ variant. The magnetic ordering temperatures T_{N1} and T_M is indicated by an arrow. (c) Low temperature $\rho(T)$ under applied magnetic fields $H = 0$–9 T applied parallel to the *c*-axis for the ThCr$_2$Si$_2$ variant. The magnetic ordering temperature T_{N2} is indicated by an arrow.
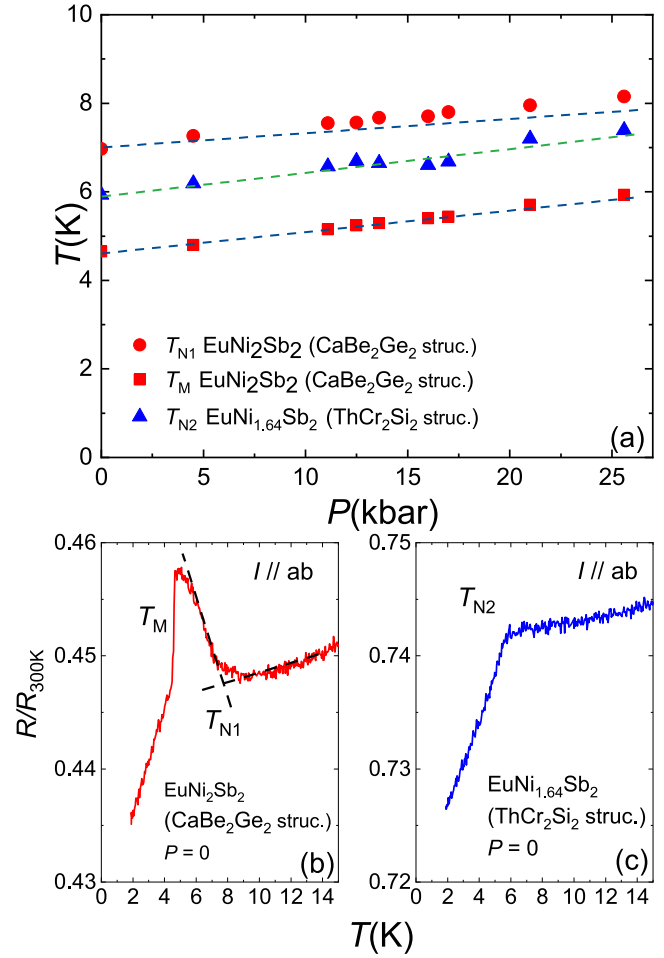
Figure 7. (a) Temperature T vs pressure P phase diagram from electrical resistance $R(T)$ measurements. (b) and (c) R/R_{300} vs T measurements for EuNi$_2$Sb$_2$ variants at ambient pressure.

thermal relaxation curves (figure 5(b)) provide evidence for a latent heat; i.e., by comparison to a typical temperature vs time response to a heat pulse, $T(t)$ near T_M is distorted by the latent heat (figure 5(b)). In order to extract the heat capacity in this temperature range, the data were analyzed using a single slope curve analysis method. Below the phase transitions C/T initially remains roughly constant and then rapidly decreases at lower T, consistent with the behavior of other divalent Eu intermetallics with similar crystalline lattices [30, 31]. We additionally point out that it is difficult to estimate the electronic coefficient of the heat capacity γ due to the large magnetic contribution from the f-electrons. However, given that the f-states are well localized we infer that $\gamma < 10$ mJ mol^{-1} K^{-2}, similar to LaPd$_2$Sb$_2$ [33].

The 4f contribution to the entropy S_{4f} is shown in figure 5(c), which was calculated by subtracting the electronic and lattice components that were obtained from the above fit and integrating C/T for temperatures 0.4 K $\leqslant T \leqslant$ 10 K. The horizontal dashed line is the expected magnetic entropy given

by the expression $S_{4f} = R \ln(2S + 1) = R \ln 8$, where R is the ideal gas constant and $S = 7/2$. S_{4f} recovers most of this value by the Néel temperature for both variants, and the small reduction of S_{4f} from the theoretical value may be partly related to the lower integration limit ($T \approx 0.4$ K) not extending to zero temperature or some uncertainty in the lattice subtraction. On the other hand, we note that $C(T)$ deviates from the Debye fit starting near 20–30 K, which is also where $\chi(T)$ begins to show a small anisotropy. This may imply that fluctuations of the order parameters extend this high, and full recovery of $S_{4f} = R \ln 8$ would require integration into this temperature range.

The *ab*-plane electrical resistivity $\rho(T)$ data are shown in figure 6. As expected for a typical metal, $\rho(T)$ for both compounds decreases monotonically from room temperature down to the Néel temperatures. The influence of disorder is seen in the relative sizes of ρ for each compound; $\rho_{300K} \approx 90$ $\mu\Omega$ cm and 54 $\mu\Omega$ cm for the ThCr$_2$Si$_2$ and CaBe$_2$Ge$_2$ variants, respectively. This trend is also evident at low temperatures, where the residual resistivities ρ_0 are 65 and 14.5 $\mu\Omega$ cm. The large ρ_0 for the ThCr$_2$Si$_2$ variant is consistent with there being substantial scattering from disorder on the Ni site due

to vacancies. Distinct behavior is then observed upon entering the antiferromagnetically ordered states. For the $CaBe_2Ge_2$ variant there is a cusp-like minimum at T_{N1}, but this is followed by a sharp reduction at T_M that signals the removal of spin scattering of conduction electrons (figure 6(b)). This is similar to what was earlier observed for the isoelectronic structural analogue $EuPd_2Sb_2$ [30]. In contrast, there is a knee-like reduction of ρ at T_{N2} that is typical for a second order antiferromagnetic phase transition (figure 6(c)). For both variants, $\rho(T)$ measurements for $T > 10$ mK show that that there are no additional phase transitions at lower temperatures. In order to probe the magnetically ordered states, $\rho(T)$ measurements were also performed with different magnetic fields applied along the *c*-axis. Here we find that the magnetic ordering temperatures are suppressed with increasing H, consistent with the $M(H)$ measurements.

Finally, results from $\rho(T)$ curves collected under pressures up to $P = 2.6$ GPa are shown in figure 7. For $T > T_N$, all of the curves exhibit metallic behavior and show a weak P dependence. For the $CaBe_2Ge_2$-type specimen that was used for this measurement, the feature at T_{N1} appears as a well defined minimum in ρ, and for both materials the magnetically ordered states retain their characteristic shapes up to the highest P. All three phase transitions increase with increasing pressure with the slopes 0.51 K GPa^{-1} (T_{12}), 0.45 K GPa^{-1} (T_M), and 0.55 K GPa^{-1} (T_{N2}). This suggests that the RKKY mediated antiferromagnetic interactions between the Eu ions are strengthened as applied pressure reduces the interatomic distances and also that these systems are distant from any valence instability.

4. Discussion and conclusions

These results reveal that the $EuNi_{2-\delta}Sb_2$ compounds are an environment in which to study the relationship between crystalline structure, electronic behavior, and europium magnetism. In particular, $\chi(T)$ shows that both systems exhibit Curie–Weiss temperature dependences that indicate an antiferromagnetic exchange interaction between nearly divalent europium ions, while $C(T)$ and $S_{4f}(T)$ are consistent with expectations for divalent europium. Distinct magnetic states are observed at low temperatures; while the $CaBe_2Ge_2$ variant first orders antiferromagnetically near $T_{N1} = 6.9$ K and then undergoes a first order phase transition at $T_M = 4.6$ K, the $ThCr_2Si_2$-variant exhibits antiferromagnetic ordering at $T_{N2} = 5.6$ K. The most closely related isoelectronic relatives $EuNi_2As_2$ ($ThCr_2Si_2$) and $EuPd_2Sb_2$ ($CaBe_2Ge_2$) exhibit analogous differences: the former shows a single antiferromagnetic phase transition while the latter shows two [30–32]. From this we infer that the distinct environments that surround the europium atoms for the two structural variants are the main factor that determines the magnetic ordering behavior. The Ni site vacancies that are seen for the $ThCr_2Si_2$ version are also of interest, but more systematic studies of their origin and impact are still needed. For example, it is possible that they are promoted by weaker bonding between the nickel atoms (as compared to the stronger Eu–Sb interactions) or from an instability of the electronic structure of the

square net of nickel atoms [34, 35]. Electronic structure calculations are needed to investigate these possibilities and to compare to the $CaBe_2Ge_2$ analogue where no vacancies are observed. We also note that an earlier work by Pöttgen shows that variation of x has a minor effect on the magnetic properties compared to what is reported here [29]. The evolution of the ordering temperatures under applied pressure also indicate that the systems are distant from a europium valence instability and that the RKKY interaction is strengthened as the lattice is compressed.

The full magnetic complexity is further revealed by considering the influence of applied magnetic fields, which induce several metamagnetic phase transitions that depend both on the structure type and the direction of H with respect to the crystallographic axes. Qualitatively similar behavior was earlier seen for the analogues $EuNi_2As_2$ ($ThCr_2Si_2$) and $EuPd_2Sb_2$ ($CaBe_2Ge_2$) [30, 32], and it remains of interest to develop a more detailed knowledge of the order parameters (e.g., using neutron scattering or nuclear magnetic resonance) and the T–H phase diagrams.

Finally, we note that these observations open several interesting directions that would be enabled by metallurgical control of the crystallographic phase. Amongst the closely related lanthanide-based 122 compounds, there are a multitude of examples that form in the $ThCr_2Si_2$ structure and we speculate that for some of these it might be possible to stabilize the $CaBe_2Ge_2$ variant following our method. Also noteworthy is that the compounds $LnNi_{2-x}Sb_2$ (Ln = La, Ce, Pr, Nd, Sm, Gd, Tb, Dy, Ho, Er) forming in the $CaBe_2Ge_2$ structure might be driven towards full Ni-site occupancy in the same way [24]. In order to make progress in this direction it will be necessary to develop a quantitative understanding of why the introduction of phosphorus encourages one structural phase over the other.

ORCID iDs

R E Baumbach https://orcid.org/0000-0002-6314-3629

References

[1] Shatruk M 2019 *J. Solid State Chem.* **272** 198–209
[2] Jeevan H S, Hossain Z, Kasinathan D, Rosner H, Geibel C and Gegenwart P 2008 *Phys. Rev.* B **78** 092406

[3] Wada H, Hundley M F, Movshovich R and Thompson J D 1999 *Phys. Rev.* B **59** 1141

[4] Onuki Y *et al* 2017 *Phil. Mag.* **97** 3399–414

[5] Stewart G R 2001 *Rev. Mod. Phys.* **73** 797–855

[6] Löhneysen H v, Rosch A, Vojta M and Wölfle P 2007 *Rev. Mod. Phys.* **79** 1015–75

[7] Gegenwart P, Si Q and Steglich F 2008 *Nat. Phys.* **4** 186–97

[8] Pfleiderer C 2009 *Rev. Mod. Phys.* **81** 1551–624

[9] Sampathkumaran E V, Gupta L C, Vijayaraghavan R, Gopalakrishnan K V, Pillay R G and Devare H G 1981 *J. Phys. C: Solid State Phys.* **14** L237

[10] Kemly E, Croft M, Murgai V, Gupta L C, Godart C, Parks R D and Segre C U 1985 *J. Magn. Magn. Mater.* **47** 403–6

[11] Hossain Z, Trovarelli O, Geibel C and Steglich F 2001 *J. Alloys Compd.* **323–324** 396–9

[12] Mitsuda A, Hamano S, Araoka N, Yayama H and Wada H 2012 *J. Phys. Soc. Japan* **81** 023709

[13] Honda F *et al* 2016 *J. Phys. Soc. Japan* **85** 063701

[14] Hiranaka Y *et al* 2013 *J. Phys. Soc. Japan* **82** 083708

[15] Wada H, Tanabe K, Yamamoto I and Mitsuda A 2019 *Solid State Commun.* **300** 113665

[16] Seiro S and Geibel C 2011 *J. Phys.: Condens. Matter.* **23** 375601

[17] Takeuchi T *et al* 2018 *J. Phys. Soc. Japan* **87** 074709

[18] Iha W *et al* 2018 *J. Phys. Soc. Japan* **87** 064706

[19] Doniach S 1977 *Physica* B + C **91** 231–4

[20] Kondo J 1964 *Prog. Theor. Phys.* **32** 37–49

[21] Ruderman M A and Kittel C 1954 *Phys. Rev.* **96** 99–102

[22] Kasuya T 1956 *Prog. Theor. Phys.* **16** 45–57

[23] Yosida K 1957 *Phys. Rev.* **106** 893–8

[24] Hofmann W K and Jeitschko W 1988 *J. Less-Common Met.* **138** 313–22

[25] Mathieu J 2013 Flux synthesis of Zintl phases and FeAs related intermetallics *PhD Thesis* Florida State University

[26] Hooft R 1996 *COLLECT* (Delft: BV Nonius)

[27] Sheldrick G 1998 *Apex II* (Madison, WI: Bruker-AXS)

[28] Sheldrick G M 2008 A short history of Shelx *Acta Crystallogr.* A **64** 112–22

[29] Schellenberg I, Eul M and Pöttgen R 2011 *Z. Naturforsch.* **66b** 1179–82

[30] Das S, McFadden K, Singh Y, Nath R, Ellern A and Johnston D C 2010 *Phys. Rev.* B **81** 054425

[31] Bauer E D, Ronning F, Scott B L and Thompson J D 2008 *Phys. Rev.* B **78** 172504

[32] Jin W T, Qureshi N, Bukowski Z, Xiao Y, Nandi S, Babij M, Fu Z, Su Y and Brückel Th 2019 *Phys. Rev.* B **99** 014425

[33] Ganesanpotti S, Yajima T, Tohyama T, Li Z, Nakano K, Nozaki Y, Tassel C, Kobayashi Y and Kageyama H 2014 *J. Alloys Compd.* **583** 151

[34] Gray D L, Francisco M C and Kanatzidis M G 2008 *Inorg. Chem.* **47** 7243

[35] Peter S C, Chondroudi M, Malliakas C D, Balasubramanian M and Kanatzidis M G 2011 *J. Am. Chem. Soc.* **133** 13840–3